

Isotropic wavevector domain image filters by a photonic crystal slab device

CHENG GUO,¹ MENG XIAO,²  MOMCHIL MINKOV,² YU SHI,² AND SHANHUI FAN^{2,*}

¹Department of Applied Physics, Stanford University, Stanford, California 94305, USA

²Ginzton Laboratory and Department of Electrical Engineering, Stanford University, Stanford, California 94305, USA

*Corresponding author: shanhui@stanford.edu

Received 27 May 2018; revised 23 August 2018; accepted 24 August 2018; posted 24 August 2018 (Doc. ID 332686); published 13 September 2018

We show that several types of isotropic image filters in the wavevector domain can be implemented with a single photonic crystal slab device. Such a slab is designed so that the guided resonance near the Γ point exhibits an isotropic band structure. Depending on the light frequency and the choice of transmission or reflection mode, the device realizes isotropic high-pass, low-pass, band-reject, and band-pass filtering in wavevector space. These filter functions are important for various image processing tasks, including edge detection, smoothing, white noise suppression, and suppression or extraction of periodic noises. We numerically demonstrate these filter functionalities by simulations of a slab structure that is designed to operate in the visible wavelength range. Our work expands the application of nanophotonics-based optical analog computing for image processing. © 2018 Optical Society of America

OCIS codes: (050.5298) Photonic crystals; (100.1160) Analog optical image processing.

<https://doi.org/10.1364/JOSAA.35.001685>

1. INTRODUCTION

Filtering in the wavevector domain is widely used in image processing [1,2]. Due to the two-dimensional nature of images, isotropic filters, where the responses depend on the magnitude but not the orientation of the wavevectors, are particularly useful. The most commonly used isotropic filters are high-pass, low-pass, band-reject, and band-pass filters, all defined in the wavevector domain [3].

In conventional Fourier optics, to achieve filtering in the wavevector domain, one first obtains a Fourier transformation of an image on a Fourier plane by passing the image through a lens. One then performs spatial filtering on the Fourier plane, followed by a Fourier transformation again through a second lens [4,5]. Such a technique requires long propagation distance and therefore results in a bulky system [6–9].

In recent years, there has been significant progress in using nanophotonic structures to develop a compact device for analog optical computing [10,11]. Specifically, many efforts have been made on achieving spatial differentiation of an incoming image, which in fact corresponds to a high-pass filter in the wavevector domain [11–22]. While most initial works on nanophotonic structures have focused on demonstrating one-dimensional differential operators, more recent works have shown that two-dimensional differential operators, including, in particular, the Laplace operator, which is a high-pass filter, can be achieved using nanophotonic structures in either reflection [23] or transmission [24].

Building upon our previous work of Ref. [24], in this paper, we show that the same class of structures, but with different operating conditions, can be used to implement many other important wavevector domain filtering functionalities, including low-pass, band-reject, and band-pass filters. These filters can be used for a variety of functions in image processing, including suppression of periodic or white noises, and image smoothing. Furthermore, in this paper, we redesign the structure using Si_3N_4 instead of Si or GaAs as originally considered in Ref. [24] to extend the operation wavelength to the visible region.

The image processing tasks that we considered here in this paper can certainly be implemented using electronic digital computing. However, nowadays there are many big-data applications that require real-time and high-throughput image processing, for which it is of interest to develop techniques to perform these computations with reduced energy consumption and increased speed [25,26]. The devices considered here may overcome this challenge by offering high-throughput image filtering directly in the optical domain, with almost no energy consumption other than the inherent optical loss associated with the corresponding operators, using structures that are compact. As such, our work indicates some of the new opportunities for optical analog computing as provided by nanophotonic structures.

2. THEORETICAL ANALYSIS

The purpose of filtering in the wavevector domain is to transform an image by modifying its Fourier transformation [27].

In general, for a normally incident light beam along the z axis with a transverse field profile $S_{\text{in}}(x, y)$, the transmitted or reflected beam has a profile $S_{\text{out}}(x, y) = \mathcal{F}^{-1}[H(k_x, k_y)\tilde{S}_{\text{in}}(k_x, k_y)]$, where \mathcal{F}^{-1} is the inverse Fourier transform, $\tilde{S}_{\text{in}}(k_x, k_y)$ is the Fourier transform of the input image, and $H(k_x, k_y)$ is the filter transfer function [1]. If $H(k_x, k_y) = H(|\mathbf{k}|)$ only depends on the magnitude of the wavevector $|\mathbf{k}|$, the filter is isotropic. Here, $\mathbf{k} = (k_x, k_y)$ refers to the in-plane wavevector.

In this paper, the isotropic filters are realized by a photonic crystal slab device, as shown in Fig. 1. This photonic crystal slab exhibits a nontrivial isotropic band structure near the Γ point. The design details for such a photonic crystal slab have been discussed in Ref. [24]. Reference [24] uses either Si or GaAs for the design, which is applicable only in the infrared wavelength range. Here, we follow the same principle to design a structure that can operate in the visible wavelength range. The dielectric constant of the material for the slabs is $\epsilon = 4.67$, which approximates that of Si_3N_4 in the visible wavelength range. Here, we use a dielectric constant that is real, as the extinction coefficient of Si_3N_4 at a visible wavelength is negligible. The photonic crystal slab has a thickness of $d = 0.50a$ and a square lattice of air holes with radii $r = 0.11a$, where a is the lattice constant. The thickness d and radius r are chosen to realize isotropic bands of guided resonances. A uniform dielectric slab with a thickness $d_s = 0.12a$ is placed in the vicinity of the photonic crystal slab. The air gap between the two slabs has a thickness $d_g = 1.93a$. d_s and d_g are chosen to set the background transmission to be unity. As a side note,

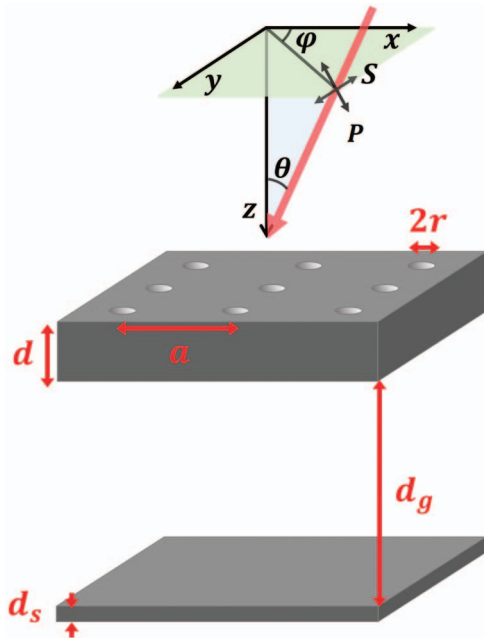


Fig. 1. Geometry of the device, which consists of a photonic crystal slab with a square lattice of air holes, separated from a uniform dielectric slab by an air gap. The slabs have a dielectric constant $\epsilon = 4.67$. The geometry parameters are $d = 0.50a$, $r = 0.11a$, $d_s = 0.12a$, $d_g = 1.93a$, where a is the lattice constant. The coordinate system is shown above the device. The red arrow indicates the direction of the incident light. The electric field directions of the S - and P -polarized light are also indicated.

the two-layer structure we use in the paper is quite compact. For a resonant wavelength $\lambda = 500$ nm, $a = 650$ nm, the total thickness is $d + d_g + d_s = 1.66$ μm . Such a structure can be fabricated using, e.g., focused ion beam assisted laser interference lithography [28].

The photonic crystal slab in Fig. 1 hosts a pair of guided resonances, which are degenerate at the Γ point with a frequency $\omega_0 = 0.77098 \times 2\pi c/a$. In general, in the vicinity of the Γ point, the band structure is highly anisotropic in the \mathbf{k} space, as has been derived in Ref. [24], assuming only the C_{4v} symmetry of the structure. However, remarkably, with the carefully tuned geometry parameters above, both bands of the guided resonances exhibit almost complete circular symmetry in the real part of the eigenfrequencies:

$$\omega_{\pm}(\mathbf{k}) \approx \omega_0 + A_{\pm}|\mathbf{k}|^2, \quad (1)$$

where $A_+ = 4.35$, $A_- = -1.41$ from fitting the band dispersion, and the upper (lower) sign corresponds to the upper (lower) band. In Eq. (1), and throughout the rest of the paper, the wavevector will be in units of $2\pi/a$.

The nearly isotropic photonic band structure ($\omega_{\pm}(\mathbf{k}) - \omega_0$) for the structure shown in Fig. 1 is plotted in Figs. 2(a), 2(c), and 2(d). Figure 2(a) shows that for both bands, the dispersions along the $\Gamma - M$ and $\Gamma - X$ directions have almost identical effective masses. Here, the effective mass tensor is defined as $m_{ij}^* = \hbar[\partial^2\omega(\mathbf{k})/\partial k_i\partial k_j]^{-1}$. Figures 2(c) and 2(d) show that the constant frequency contours for both bands are almost circular. We note that the radiative linewidths $\gamma_{\pm}(\mathbf{k})$, unlike $\omega_{\pm}(\mathbf{k})$, are anisotropic. Nonetheless, $(\gamma_{\pm}(\mathbf{k}) - \gamma_0)$ are much smaller than $(\omega_{\pm}(\mathbf{k}) - \omega_0)$, thus, they do not affect the circular symmetry of the transfer functions much, as we will show later. (See also Supplement of Ref. [24].)

In general, guided resonances in photonic crystal slabs may induce sharp Fano resonance features in the transmission and reflection spectra [29–32]. For the specific pair of guided resonances considered here, it has been proved in Ref. [24] that, due to the isotropic band structure, S -polarized (P -polarized) light can only excite the upper (lower) band for every direction of incidence. This effect is referred to as *single-band excitation*.

Due to the single-band excitation effect, as well as the presence of the uniform dielectric slab, which sets the background transmission coefficient [30] to be unity, for this structure shown in Fig. 1, the transmission and reflection coefficients are

$$t_{\pm}(\omega, \mathbf{k}) = \frac{i[\omega - \omega_{\pm}(\mathbf{k})]}{i[\omega - \omega_{\pm}(\mathbf{k})] + \gamma_{\pm}(\mathbf{k})}, \quad (2)$$

$$r_{\pm}(\omega, \mathbf{k}) = -e^{i\phi} \frac{\gamma_{\pm}(\mathbf{k})}{i[\omega - \omega_{\pm}(\mathbf{k})] + \gamma_{\pm}(\mathbf{k})}, \quad (3)$$

where the upper (lower) sign corresponds to S -polarized (P -polarized) light and upper (lower) band; ω is the incident light frequency. Therefore, on resonance,

$$t_{\pm}(\omega_{\pm}(\mathbf{k}), \mathbf{k}) = 0, \quad r_{\pm}(\omega_{\pm}(\mathbf{k}), \mathbf{k}) = -e^{i\phi}. \quad (4)$$

The numerically determined transmission and reflection spectra for S -polarized light are plotted in Figs. 2(e) and 2(f). Due to the effect of single-band excitation, S -polarized light only excites the upper band of guided resonances. Moreover,

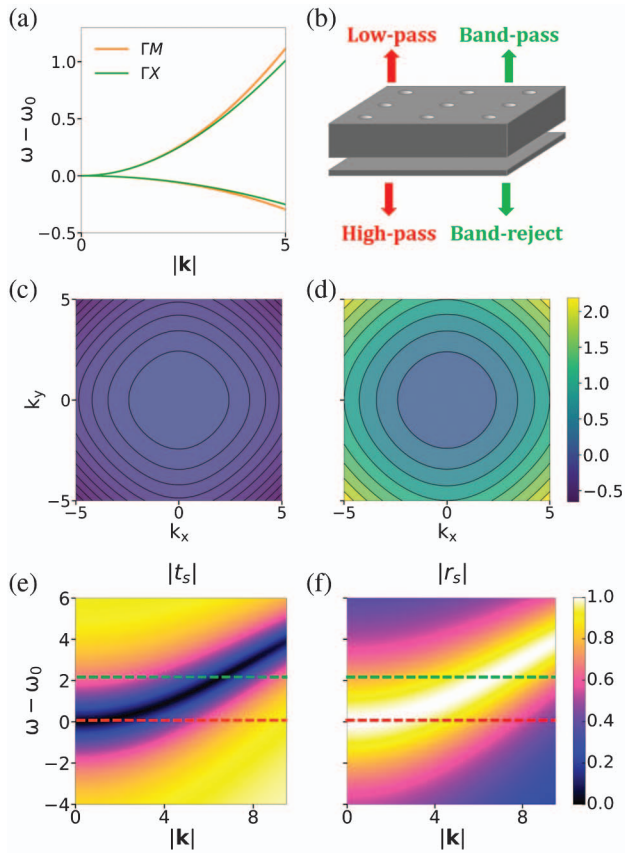


Fig. 2. (a), (c), (d) Nearly isotropic photonic band structure of the photonic crystal slab shown in Fig. 1 near the frequency $\omega_0 = 0.77098 \times 2\pi c/a$. (a) Band dispersions along Γ -X and Γ -M directions. (c) Constant frequency contours of the lower band. (d) Constant frequency contours of the upper band. (b) Scheme of multiple filtering functions of the device. When the light frequency is on resonance at the normal incidence [$\omega = \omega_0$, labeled by red arrows in (b) and red horizontal lines in (e), (f)], the device realizes an isotropic high-pass filter (Laplacian) at transmission and low-pass filter at reflection. When the light frequency is detuned from the resonance at the normal incidence [$\omega = \omega_k$, labeled by green arrows in (b) and green horizontal lines in (e), (f)], the device realizes an isotropic band-reject filter at transmission and band-pass filter at reflection. (e) Transmittance $|t|$ for S-polarized light as a function of ω and $|\mathbf{k}|$ near $\omega_0 = 0.77098 \times 2\pi c/a$ along a general wavevector direction ($\varphi = 14^\circ$). Due to the isotropic band structure, S light only excites the upper band, and the transmission spectra are almost identical along any wavevector direction φ . $|t| = 0$ when $\omega = \omega(\mathbf{k})$. (f) Reflectance $|r|$ for S-polarized light as a function of ω and $|\mathbf{k}|$ near $\omega_0 = 0.77098 \times 2\pi c/a$ along a general wavevector direction ($\varphi = 14^\circ$). The reflection spectra are identical along any wavevector direction. $|r| = 1$ when $\omega = \omega(\mathbf{k})$. In all of the plots, frequency $(\omega - \omega_0)$ is in units of $10^{-4} \times 2\pi c/a$, while $|\mathbf{k}|$, k_x , and k_y are in units of $10^{-3} \times 2\pi/a$.

as expected from Eqs. (1)–(3), the resultant transmission and reflection spectra are isotropic, i.e., the spectra are identical along any wavevector direction as defined by the azimuthal angle φ in Fig. 1. When $\omega = \omega(\mathbf{k})$, the transmittance exhibits sharp dips with $|t| = 0$, while the reflectance exhibits peaks with $|r| = 1$, as expected from Eq. (4).

Depending on the operating conditions, the structure as shown in Fig. 1 can be used to perform several very useful image processing functionalities.

A. Isotropic High-Pass Filter

In our previous work of Ref. [24], we studied the \mathbf{k} -dependent transmittance at the frequency $\omega = \omega_0 \equiv \omega_\pm(k = 0)$:

$$|t_\pm(\omega_0, \mathbf{k})| = \frac{|\omega_\pm(\mathbf{k}) - \omega_0|}{\sqrt{[\omega_\pm(\mathbf{k}) - \omega_0]^2 + \gamma_\pm(\mathbf{k})^2}} \quad (5)$$

$$\approx \frac{|\omega_\pm(\mathbf{k}) - \omega_0|}{\gamma_0} = \frac{A_\pm}{\gamma_0} |\mathbf{k}|^2. \quad (6)$$

This transmittance realizes the Laplacian, a special isotropic high-pass filter.

In this paper, we show that the same device can provide a few other very useful image processing functionalities under different operating conditions.

B. Isotropic Low-Pass Filter

At the frequency $\omega = \omega_0$, if one considers instead the reflected light, the transfer function is

$$|r_\pm(\omega_0, \mathbf{k})| = \frac{1}{\sqrt{1 + [\omega_\pm(\mathbf{k}) - \omega_0]^2 / \gamma_\pm(\mathbf{k})^2}} \approx \frac{1}{\sqrt{1 + A_\pm^2 |\mathbf{k}|^4 / \gamma_0^2}}. \quad (7)$$

This transfer function realizes an isotropic low-pass filter with reflection peak $|r_\pm| = 1$ at the Γ point.

C. Isotropic Band-Reject Filter

Suppose instead we operate away from the frequency ω_0 , but at the frequency $\omega = \omega_{\pm,q}$, where q is the amplitude of a non-zero in-plane wavevector, the transfer function then becomes

$$|t_\pm(\omega_{\pm,q}, \mathbf{k})| = \frac{|\omega_\pm(\mathbf{k}) - \omega_{\pm,q}|}{\sqrt{[\omega_\pm(\mathbf{k}) - \omega_{\pm,q}]^2 + \gamma_\pm(\mathbf{k})^2}}. \quad (8)$$

This transfer function realizes an isotropic band-reject filter with transmission dip $|t_\pm| = 0$ at $|\mathbf{k}| = q$.

D. Isotropic Band-Pass Filter

At the frequency $\omega = \omega_{\pm,q}$ the reflection has a transfer function

$$|r_\pm(\omega_q, \mathbf{k})| = \frac{1}{\sqrt{1 + [\omega_\pm(\mathbf{k}) - \omega_{\pm,q}]^2 / \gamma_\pm(\mathbf{k})^2}}. \quad (9)$$

This transfer function realizes an isotropic band-pass filter with reflection peak $|r_\pm| = 1$ at $|\mathbf{k}| = q$.

Therefore, our device achieves multiple filtering functions. As schematically shown in Fig. 2(b), when the light frequency is on resonance at normal incidence ($\omega = \omega_0$), the device operates as an isotropic high-pass filter (Laplacian) at the transmission mode and an isotropic low-pass filter at the reflection mode. When the light frequency is detuned a bit from the resonance at normal incidence, the device operates as an isotropic

band-reject filter at the transmission mode and an isotropic band-pass filter at the reflection mode, where the rejected or passed wavevector components are determined by the light frequency detuning and polarization. For transmission mode, the transmitted image is the required filtered result. For reflection mode, the reflected image is the required filtered result, which can be separated from the incident image by using a beam splitter.

3. NUMERICAL DEMONSTRATION

Now, we numerically demonstrate the filtering functions of our device. The isotropic high-pass filter (Laplacian) has been studied in detail in Ref. [24]. Here, since the physical structure is different, we include a brief discussion of the performance of this device as a Laplacian for completeness, but focus on the other three isotropic filters.

In all the numerical demonstrations below, the incident beam is *S* polarized. The transmitted image is calculated following the standard way in image processing [1]. (1) Compute the Fourier transform $\tilde{S}_{in}(k_x, k_y)$ of the incident field profile $S_{in}(x, y)$. Note the incident image is $|S_{in}(x, y)|^2$. (2) Compute the Fourier transform of the output field profile, $\tilde{S}_{out}(k_x, k_y) = H(k_x, k_y)\tilde{S}_{in}(k_x, k_y)$, where $H(k_x, k_y)$ is the transfer function. (3) Obtain the output field profile $S_{out}(x, y)$ by inverse Fourier transform. Calculate the output image $|S_{out}(x, y)|^2$.

A. Isotropic High-Pass Filter (the Laplacian)

Figure 3 illustrates the isotropic high-pass filter (the Laplacian). Figure 3(a) plots the filter transfer function: the transmittance for *S*-polarized light $|t_s|(k_x, k_y)$ at the frequency $\omega_0 = 0.77098 \times 2\pi c/a$. The transfer function is almost isotropic. Figure 3(b) plots $|t_s|$ as a function of $|k|$ along a general wavevector direction ($\varphi = 14^\circ$), and the fitting result using Eqs. (5) and (6), respectively. The fitting of Eq. (5) is almost perfect in the wavevector range as shown, while the quadratic fitting using Eq. (6) is very good for $|k|$ up to $0.6 \times 10^{-2} \times 2\pi/a$. These plots confirm that the device indeed operates as an isotropic high-pass filter (the Laplacian) in this case. In Fig. 3(a) [and also in Fig. 4(a), as shown later], at larger wavevectors, the transfer function exhibits some anisotropy due to the dependency of the radiative linewidth $\gamma(k)$ on the direction of k .

The Laplacian enables image sharpening and edge detection [24]. Figure 3(e) shows an incident image of the Stanford emblem, while Fig. 3(c) plots the Fourier transform of the field profile for this incident image. Figure 3(d) shows the calculated Fourier spectrum for the transmitted image, which is obtained by a pointwise product of Figs. 3(a) and 3(c). The low wavevector components have been filtered out. Figure 3(f) is the calculated transmitted image, which shows all the edges with different orientations.

B. Isotropic Low-Pass Filter

Figure 4 illustrates the isotropic low-pass filter. Figure 4(a) plots the filter transfer function: the reflectance for *S*-polarized light $|r_s|(k_x, k_y)$ at the frequency $\omega_0 = 0.77098 \times 2\pi c/a$. The transfer function is almost isotropic. Figure 4(b) plots $|r_s|$ as a function of $|k|$ along a general wavevector direction ($\varphi = 14^\circ$) and the fitting result of Eq. (7). The fitting is almost perfect in the

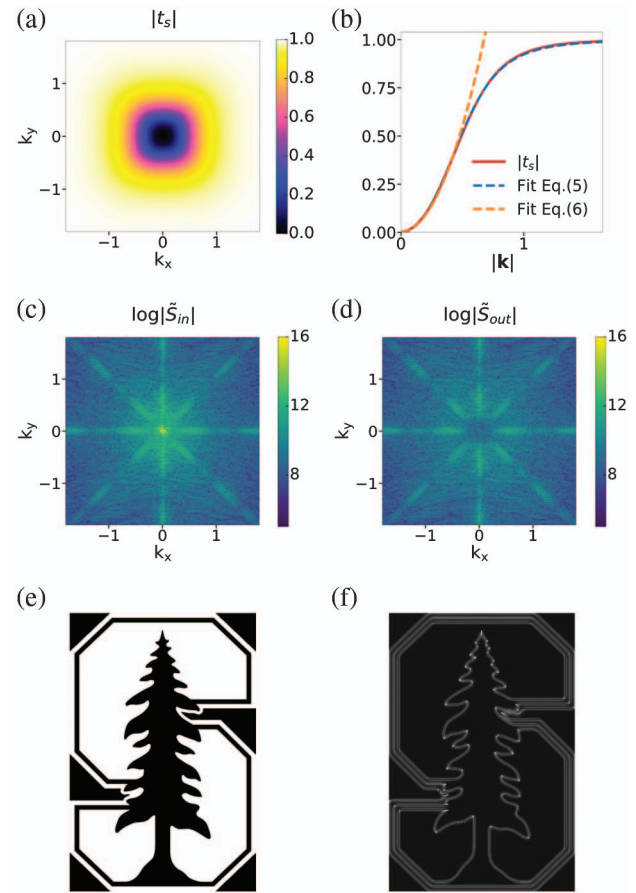


Fig. 3. Isotropic high-pass filter (Laplacian). (a) Transmittance for *S*-polarized light $|t_s|(k_x, k_y)$ at the frequency $\omega_0 = 0.77098 \times 2\pi c/a$. (b) $|t_s|$ as a function of $|k|$ along a general wavevector direction ($\varphi = 14^\circ$). (c) Log plot of the Fourier transform of the field profile for the incident image (e): $\log|\tilde{S}_{in}|(k_x, k_y)$. (d) Log plot of the Fourier transform of the field profile for the reflected image (f): $\log|\tilde{S}_{out}|(k_x, k_y)$. The low wavevector components have been filtered out. (e) Incident image $|S_{in}|^2$ of the Stanford emblem. The image size is $5220a \times 3456a$. (f) Calculated transmitted image $|S_{out}|^2$, which shows the edges with different orientations. $|k|$, k_x , and k_y are in units of $10^{-2} \times 2\pi/a$.

wavevector range as shown. These plots confirm that the device indeed operates as an isotropic low-pass filter in this case.

The isotropic low-pass filter accomplishes image smoothing, with applications ranging from character recognition in machine perception, preprocessing functions in the printing and publishing industry, to satellite and aerial image processing [1,33]. Here, we show one specific application of the low-pass filter in white noise reduction. Figure 4(e) shows an incident image of the Stanford emblem corrupted by white noise, while Fig. 4(c) plots the Fourier transform of the field profile for this incident image. Figure 4(d) shows the calculated Fourier spectrum for the reflected image, which is obtained by a pointwise product of Figs. 4(a) and 4(c). The high wavevector components have been filtered out. Figure 4(f) shows the calculated reflected image, where the white noise has indeed been reduced, demonstrating image smoothing.

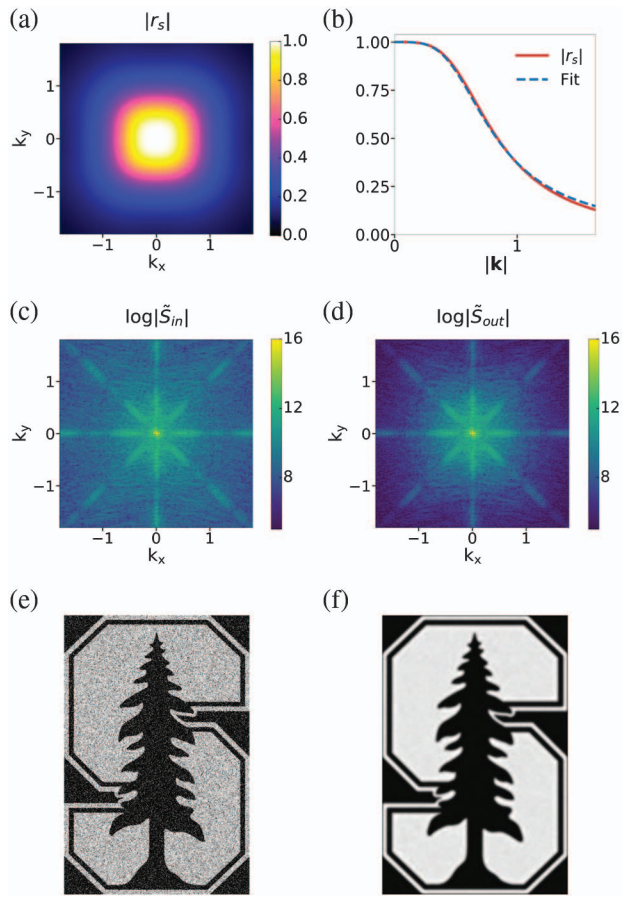


Fig. 4. Isotropic low-pass filter. (a) Reflectance for S -polarized light $|r_s|(k_x, k_y)$ at the frequency $\omega_0 = 0.77098 \times 2\pi c/a$. (b) $|r_s|$ as a function of $|\mathbf{k}|$ along a general wavevector direction ($\varphi = 14^\circ$). (c) Log plot of the Fourier transform of the field profile for the incident image (e): $\log |\tilde{S}_{in}|(k_x, k_y)$. (d) Log plot of the Fourier transform of the field profile for the reflected image (f): $\log |\tilde{S}_{out}|(k_x, k_y)$. The high wavevector components have been filtered out. (e) Incident image $|S_{in}|^2$ of the Stanford emblem corrupted by white noise. The image size is $5220a \times 3456a$. (f) Calculated reflected image $|S_{out}|^2$, which reduces the white noise by image smoothing. $|\mathbf{k}|$, k_x , and k_y are in units of $10^{-2} \times 2\pi/a$.

C. Isotropic Band-Reject Filter

Figure 5 illustrates the isotropic band-reject filter. Figure 5(a) plots the filter transfer function: the transmittance for S -polarized light $|t_s|(k_x, k_y)$ at the frequency $\omega_q = 0.77130 \times 2\pi c/a$. The transfer function is almost isotropic. Figure 5(b) plots $|t_s|$ as a function of $|\mathbf{k}|$ along a general wavevector direction ($\varphi = 14^\circ$), which shows $|t_s| = 0$ at $|\mathbf{k}| = 0.84 \times 10^{-2} \times 2\pi/a$. We fit the transmittance curve with Eq. (8) together with Eq. (1) and $\gamma(\mathbf{k}) \approx \gamma_0$. The fitting is almost perfect in the wavevector range as shown. These plots confirm that the device indeed operates as an isotropic band-reject filter in this case.

The isotropic band-reject filter can effectively eliminate periodic noise, a common type of noise arising typically from electrical or electromechanical interference during image acquisition [1,34,35]. As periodic noise appears as peaks in the Fourier transform at locations corresponding to the

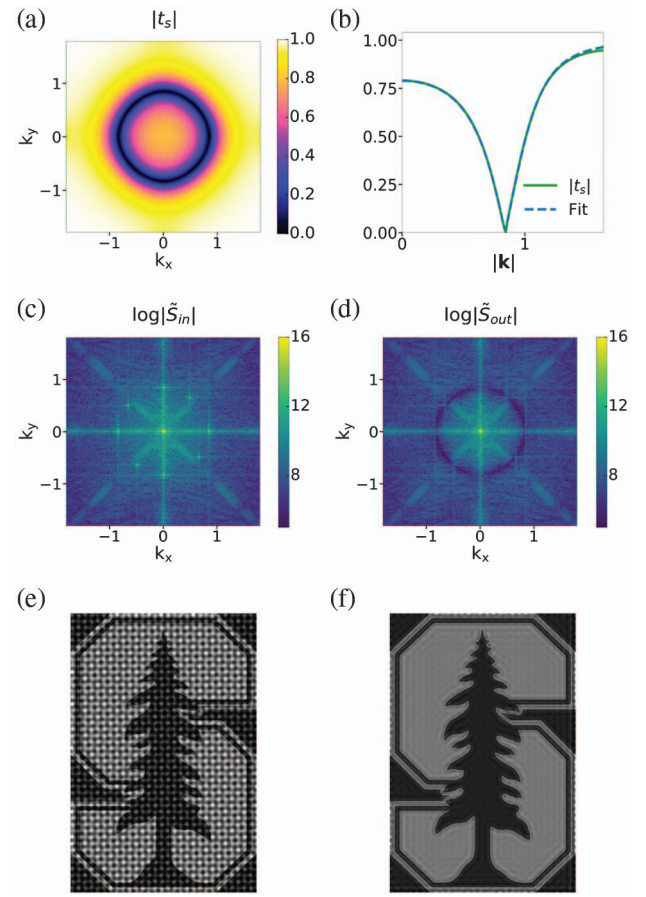


Fig. 5. Isotropic band-reject filter. (a) Transmittance for S -polarized light $|t_s|(k_x, k_y)$ at the frequency $\omega_q = 0.77130 \times 2\pi c/a$. (b) $|t_s|$ as a function of $|\mathbf{k}|$ along a general wavevector direction ($\varphi = 14^\circ$). (c) Log plot of the Fourier transform of the field profile for the incident image (e): $\log |\tilde{S}_{in}|(k_x, k_y)$. The sinusoidal noise appears as peaks in the spectrum, which lie on an approximate circle around the origin. (d) Log plot of the Fourier transform of the field profile for the transmitted image (f): $\log |\tilde{S}_{out}|(k_x, k_y)$. The wavevector components corresponding to the periodic noise have been filtered out. (e) Incident image $|S_{in}|^2$ of the Stanford emblem corrupted by sinusoidal noise. The image size is $5220a \times 3456a$. (f) Calculated transmitted image $|S_{out}|^2$, which eliminates the periodic noise. $|\mathbf{k}|$, k_x , and k_y are in units of $10^{-2} \times 2\pi/a$.

wavevectors of the periodic interference, it can be isolated and filtered by band-reject filters. Here, we show an example of periodic noise reduction with the isotropic band-reject filter. Figure 5(e) shows an incident image of the Stanford emblem corrupted by sinusoidal noise, while Fig. 5(c) plots the Fourier transform of the field profile for this incident image. The periodic noise appears as spectral peaks in the wavevector space, which lie on an approximate circle around the origin. Figure 5(d) shows the calculated Fourier spectrum for the transmitted image, which is obtained by a pointwise product of Figs. 5(a) and 5(c). The spectral peaks corresponding to the periodic noise have been filtered out. Figure 5(f) shows the calculated transmitted image, where the periodic noise has indeed been eliminated effectively. Here, we note that the rejected wavevector where the maximum rejection occurs in our

band-reject filter can be easily tuned by tuning the light frequency.

D. Isotropic Band-Pass Filter

Figure 6 illustrates the isotropic band-pass filter. Figure 6(a) plots the filter transfer function: the reflectance for S -polarized light $|r_s|(k_x, k_y)$ at the frequency $\omega_q = 0.77130 \times 2\pi c/a$. The transfer function is almost isotropic. Figure 6(b) plots $|r_s|$ as a function of $|\mathbf{k}|$ along a general wavevector direction ($\varphi = 14^\circ$), which shows $|r_s| = 1$ at $|\mathbf{k}| = 0.84 \times 10^{-2} \times 2\pi/a$. We fit the reflectance curve with Eq. (9) together with Eq. (1) and $\gamma(\mathbf{k}) \approx \gamma_0$. The fitting is almost perfect in the wavevector range as shown. These plots confirm that the device indeed operates as an isotropic band-pass filter in this case.

The isotropic band-pass filter performs the opposite operation of the band-reject filter. It is quite useful in isolating the

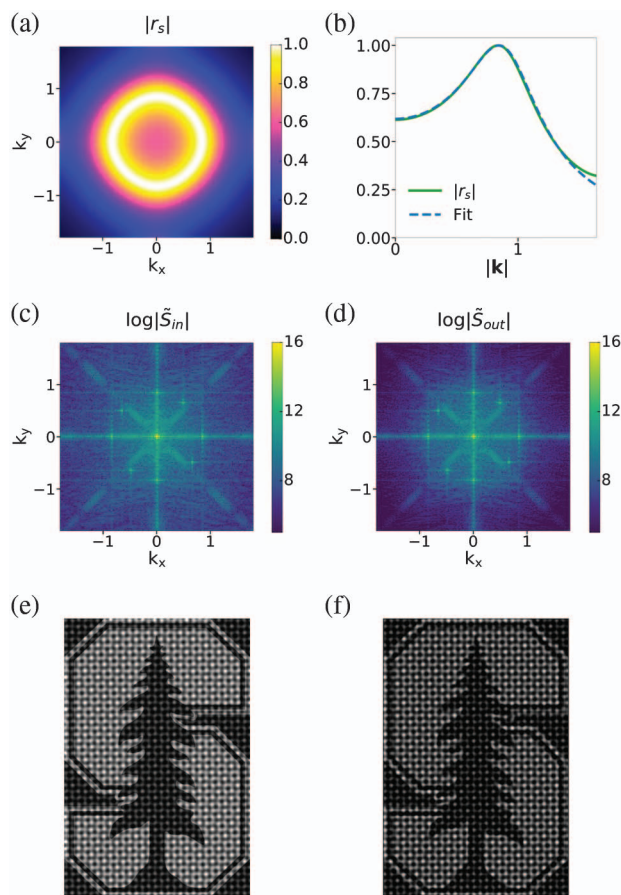


Fig. 6. Isotropic band-pass filter. (a) Reflectance for S -polarized light $|r_s|(k_x, k_y)$ at the frequency $\omega_q = 0.77130 \times 2\pi c/a$. (b) $|r_s|$ as a function of $|\mathbf{k}|$ along a general wavevector direction ($\varphi = 14^\circ$). (c) Log plot of the Fourier transform of the field profile for the incident image (e): $\log |\tilde{S}_{in}|(k_x, k_y)$. The sinusoidal noise appears as impulses in the spectrum, which lie on an approximate circle around the origin. (d) Log plot of the Fourier transform of the field profile for the reflected image (f): $\log |\tilde{S}_{out}|(k_x, k_y)$. (e) Incident image $|S_{in}|^2$ of the Stanford emblem corrupted by sinusoidal noise. The image size is $5220a \times 3456a$. (f) Calculated reflected image $|S_{out}|^2$, which isolates the periodic noise and simplifies its analysis. $|\mathbf{k}|$, k_x , and k_y are in units of $10^{-2} \times 2\pi/a$.

effects on an image caused by selected wavevector bands [1]. Here, we show an example of extracting periodic noise patterns with the isotropic band-pass filter. Figure 6(e) shows an incident image of the Stanford emblem corrupted by sinusoidal noise [same as Fig. 5(e)], while Fig. 6(c) plots the Fourier transform of the field profile for this incident image. Figure 6(d) shows the calculated Fourier spectrum for the reflected image, which is obtained by a pointwise product of Figs. 6(a) and 6(c). Figure 6(f) shows the calculated reflected image, where the periodic noise pattern is isolated and appears more clearly. This is useful because it simplifies the analysis of the noise, largely independent of the image content [1].

4. FINAL REMARKS AND CONCLUSION

Our design of isotropic wavevector domain image filters using a photonic crystal slab is based on the guided resonances with isotropic band structure. The same idea can extend to other photonic structures that host resonant modes with isotropic band structures. In particular, the phase-shifted Bragg grating in Ref. [23] can also perform the four filtering functionalities of our device, but with the transmission/reflection mode flipped.

In conclusion, we have shown that isotropic high-pass, low-pass, band-reject, and band-pass filters can be implemented at visible wavelengths using one photonic crystal slab device. Such a simple but multi-functional photonic device may find various applications involving image processing. For instance, it can be used as the first layer of image recognition systems.

Funding. Samsung Electronics; U.S. Air Force (USAF) (FA9550-17-1-0002).

Acknowledgment. The authors thank Yu Guo and Dr. Bo Zhao for helpful discussions.

REFERENCES

1. R. Gonzalez and R. Woods, *Digital Image Processing*, 3rd ed. (Prentice Hall, 2008).
2. R. L. Easton, *Fourier Methods in Imaging* (Wiley, 2010).
3. A. Rosenfeld and A. C. Kak, *Digital Picture Processing* (Academic, 1982).
4. F. T. S. Yu, S. Jutamulia, and S. Yin, *Introduction to Information Optics* (Academic, 2001).
5. J. W. Goodman, *Introduction to Fourier Optics*, 3rd ed. (Roberts and Company, 2005).
6. T. Y. Chang, J. H. Hong, and P. Yeh, "Spatial amplification: an image-processing technique using the selective amplification of spatial frequencies," *Opt. Lett.* **15**, 743–745 (1990).
7. J. Eu, C. Liu, and A. Lohmann, "Spatial filters for differentiation," *Opt. Commun.* **9**, 168–171 (1973).
8. R. Sirohi and V. R. Mohan, "Differentiation by spatial filtering," *Opt. Acta* **24**, 1105–1113 (1977).
9. D. Görlitz and F. Lanzl, "A holographic spatial filter for direction independent differentiation," *Jpn. J. Appl. Phys.* **14**, 223–228 (1975).
10. D. R. Solli and B. Jalali, "Analog optical computing," *Nat. Photonics* **9**, 704–706 (2015).
11. A. Silva, F. Monticone, G. Castaldi, V. Galdi, A. Alu, and N. Engheta, "Performing mathematical operations with metamaterials," *Science* **343**, 160–163 (2014).
12. A. Youssefi, F. Zangeneh-Nejad, S. Abdollahramezani, and A. Khavasi, "Analog computing by Brewster effect," *Opt. Lett.* **41**, 3467–3470 (2016).

13. T. Zhu, Y. Zhou, Y. Lou, H. Ye, M. Qiu, Z. Ruan, and S. Fan, "Plasmonic computing of spatial differentiation," *Nat. Commun.* **8**, 15391 (2017).
14. A. Pors, M. G. Nielsen, and S. I. Bozhevolnyi, "Analog computing using reflective plasmonic metasurfaces," *Nano Lett.* **15**, 791–797 (2015).
15. S. AbdollahRamezani, K. Arik, A. Khavasi, and Z. Kavehvash, "Analog computing using graphene-based metalines," *Opt. Lett.* **40**, 5239–5242 (2015).
16. A. Chizari, S. Abdollahramezani, M. V. Jamali, and J. A. Salehi, "Analog optical computing based on a dielectric meta-reflect array," *Opt. Lett.* **41**, 3451–3454 (2016).
17. N. V. Golovastikov, D. A. Bykov, and L. L. Doskolovich, "Resonant diffraction gratings for spatial differentiation of optical beams," *Quantum Electron.* **44**, 984–988 (2014).
18. Y. Fang, Y. Lou, and Z. Ruan, "On-grating graphene surface plasmons enabling spatial differentiation in the terahertz region," *Opt. Lett.* **42**, 3840–3843 (2017).
19. Y. Hwang, T. J. Davis, J. Lin, and X.-C. Yuan, "Plasmonic circuit for second-order spatial differentiation at the subwavelength scale," *Opt. Express* **26**, 7368–7375 (2018).
20. D. A. Bykov, L. L. Doskolovich, A. A. Morozov, V. V. Podlipnov, E. A. Bezus, P. Verma, and V. A. Soifer, "First-order optical spatial differentiator based on a guided-mode resonant grating," *Opt. Express* **26**, 10997–11006 (2018).
21. Z. Dong, J. Si, X. Yu, and X. Deng, "Optical spatial differentiator based on subwavelength high-contrast gratings," *Appl. Phys. Lett.* **112**, 181102 (2018).
22. W. Wu, W. Jiang, J. Yang, S. Gong, and Y. Ma, "Multilayered analog optical differentiating device: performance analysis on structural parameters," *Opt. Lett.* **42**, 5270–5273 (2017).
23. D. A. Bykov, L. L. Doskolovich, E. A. Bezus, and V. A. Soifer, "Optical computation of the Laplace operator using phase-shifted Bragg grating," *Opt. Express* **22**, 25084–25092 (2014).
24. C. Guo, M. Xiao, M. Minkov, Y. Shi, and S. Fan, "Photonic crystal slab Laplace operator for image differentiation," *Optica* **5**, 251–255 (2018).
25. D. L. Pham, C. Xu, and J. L. Prince, "Current methods in medical image segmentation," *Annu. Rev. Biomed. Eng.* **2**, 315–337 (2000).
26. R. J. Holyer and S. H. Peckinpaugh, "Edge detection applied to satellite imagery of the oceans," *IEEE Trans. Geosci. Remote Sens.* **27**, 46–56 (1989).
27. R. N. Bracewell, *The Fourier Transform and Its Applications* (McGraw-Hill, 1986).
28. L. Vogelaar, W. Nijdam, H. A. G. M. van Wolferen, R. M. de Ridder, F. B. Segerink, E. Flück, L. Kuipers, and N. F. van Hulst, "Large area photonic crystal slabs for visible light with waveguiding defect structures: fabrication with focused ion beam assisted laser interference lithography," *Adv. Mater.* **13**, 1551–1554 (2001).
29. T. Ochiai and K. Sakoda, "Dispersion relation and optical transmittance of a hexagonal photonic crystal slab," *Phys. Rev. B* **63**, 125107 (2001).
30. S. Fan and J. D. Joannopoulos, "Analysis of guided resonances in photonic crystal slabs," *Phys. Rev. B* **65**, 235112 (2002).
31. S. G. Tikhodeev, A. L. Yablonskii, E. A. Muljarov, N. A. Gippius, and T. Ishihara, "Quasiguided modes and optical properties of photonic crystal slabs," *Phys. Rev. B* **66**, 045102 (2002).
32. W. Zhou, D. Zhao, Y.-C. Shuai, H. Yang, S. Chuwongin, A. Chadha, J.-H. Seo, K. X. Wang, V. Liu, Z. Ma, and S. Fan, "Progress in 2D photonic crystal Fano resonance photonics," *Prog. Quantum Electron.* **38**, 1–74 (2014).
33. A. Buades, B. Coll, and J. M. Morel, "A review of image denoising algorithms, with a new one," *Multiscale Model. Simul.* **4**, 490–530 (2005).
34. I. N. Aizenberg and C. Butakoff, "Frequency domain medianlike filter for periodic and quasi-periodic noise removal," *Proc. SPIE* **4667**, 181–191 (2002).
35. M. Banham and A. Katsaggelos, "Digital image restoration," *IEEE Signal Process. Mag.* **14**(2), 24–41 (1997).